Unstable fronts and motile structures formed by microrollers

Michelle Driscoll[1]*[†], Blaise Delmotte[2]*[†], Mena Youssef[3], Stefano Sacanna[3], Aleksandar Donev[2] and Paul Chaikin[1]

Condensation of objects into stable clusters occurs naturally in equilibrium[1] and driven systems[2-5]. It is commonly held that potential interactions[6], depletion forces[7], or sensing[8] are the only mechanisms which can create long-lived compact structures. Here we show that persistent motile structures can form spontaneously from hydrodynamic interactions alone, with no sensing or potential interactions. We study this structure formation in a system of colloidal rollers suspended and translating above a floor, using both experiments and large-scale three-dimensional simulations. In this system, clusters originate from a previously unreported fingering instability, where fingers pinch off from an unstable front to form autonomous 'critters', whose size is selected by the height of the particles above the floor. These critters are a stable state of the system, move much faster than individual particles, and quickly respond to a changing drive. With speed and direction set by a rotating magnetic field, these active structures offer interesting possibilities for guided transport, flow generation, and mixing at the microscale.

We have identified a new instability in one of the most basic systems of low-Reynolds-number (steady Stokes or overdamped) flow, a collection of spheres rotating near a wall. This system has been well studied analytically and numerically[9,10], since it is considered a base model for understanding many microbial and colloidal flows. The instability visually resembles wet paint dripping down a wall or individual droplets sliding down a windshield[11]—examples of Rayleigh–Taylor instabilities[12]. However, in those and other clustering phenomena, what holds things together is surface tension or other forces deriving from an interaction potential. Here we use a model system to explore whether hydrodynamic interactions alone, without particle collisions, attractions or sense/response redirection, can lead to stable finite clusters.

The experimental system consists of polymer colloids with radius $a = 0.66\,\mu m$ which have a small permanent magnetic moment ($|\mathbf{m}| \sim 5 \times 10^{-16}\,A\,m^{-2}$) from an embedded haematite cube[13] (see schematic in Fig. 1a). Inter-particle magnetic interactions are small compared to thermal energy ($< 0.1 k_B T$). A rotating magnetic field ($\mathbf{B} = B_0 \left[\cos(\omega t)\hat{\mathbf{x}} + \sin(\omega t)\hat{\mathbf{z}} \right]$) with magnitude B_0 and frequency $f = \omega/2\pi$ is applied, causing all the particles to rotate about the **y**-axis at the same rate ω. The particles rotate synchronously with the field for $\omega < \omega_c$, where ω_c is the critical frequency above which the applied magnetic torque is not enough to balance the viscous torque on the particle (see Supplementary Section I for details of the rotation mechanism). In all of our experiments, $\omega < \omega_c$. In contrast with recent experiments on Quincke rollers[14], the rotation direction is prescribed and does not arise from the system dynamics.

Hydrodynamics is the dominant inter-particle interaction in this system, which is distinctly different from many other systems of rotating magnetic particles, where dynamics is found to be a strong function of inter-particle magnetic interactions[15-18]. Many ferromagnetic particles with a small remnant moment could produce the same behaviour. Gravity plays an unusual role in our instability. Rather than a driving force partially compensated by surface tension or viscosity, as in Rayleigh–Taylor instabilities, here gravity is completely compensated by thermal motion and sets the average particle height, $h = a + k_B T/mg$, where mg is the particle buoyant weight. The particles are contained in glass capillary chambers, with a depth $\geq 100\,\mu m$. The particles have a density of $2{,}000\,kg\,m^{-3}$, and are thus suspended at $h \approx 1.0\,\mu m$ above the capillary floor, interacting essentially with only one wall.

We model the system as particles near an infinite wall driven at a constant rotational frequency. The many-body simulations are done using an accelerated stresslet-free variant of Stokesian dynamics[19] that represents each particle as a single regularized stokeslet and rotlet singularity. The hydrodynamic interactions between the particles, and the particles and the wall, are explicitly modelled (see Methods). This is a minimally resolved, and thus low-accuracy method. The accuracy of the numerical calculations can be improved by using a 'multi-blob' approach where particles such as our rotating spheres are represented as a rigid cluster of regularized stokeslet singularities or 'blobs'[20]. The accuracy and resolution are set by the number of blobs per particle. Improved resolution comes at the computational expense of a reduction in the number of particles and the time span that can be simulated. In Supplementary Fig. 1b we compare a well-resolved sphere model containing 2,562 blobs, which is used in Fig. 1c,d, with the minimally resolved model used elsewhere, which produces qualitatively similar results. The simulations include neither the effects of thermal motion nor magnetic forces as they are small compared to viscous forces (see Supplementary Section II). The particle–wall separation is set by creating a repulsive wall potential. In addition to the hydrodynamic interactions between particles, steric repulsion between particles is used for some simulations (for example, to model the experiment) and dropped for others (for example, to test the role of pure hydrodynamics).

Hydrodynamic coupling plays a crucial role in the dynamics of this system. A sphere rotating near a wall about the **y**-axis will move in the **x**-direction (see Fig. 1c). This motion is a result of the unequal drag force on the top and the bottom of the particle. Its translation speed v_0 is set by the scaled distance to the wall and the rotation rate[10]: $v_0 = \omega a f(h/a)$, and vanishes as the height increases—that is, $f(h/a) \rightarrow 0$ as $h \rightarrow \infty$. However, as shown in Fig. 1c, v_0 is

[1]Department of Physics, New York University, New York, New York 10003, USA. [2]Courant Institute of Mathematical Sciences, New York University, New York, New York 10012, USA. [3]Department of Chemistry, New York University, New York, New York 10003, USA. [†]These authors contributed equally to this work. *e-mail: mdriscoll@nyu.edu; delmotte@courant.nyu.edu
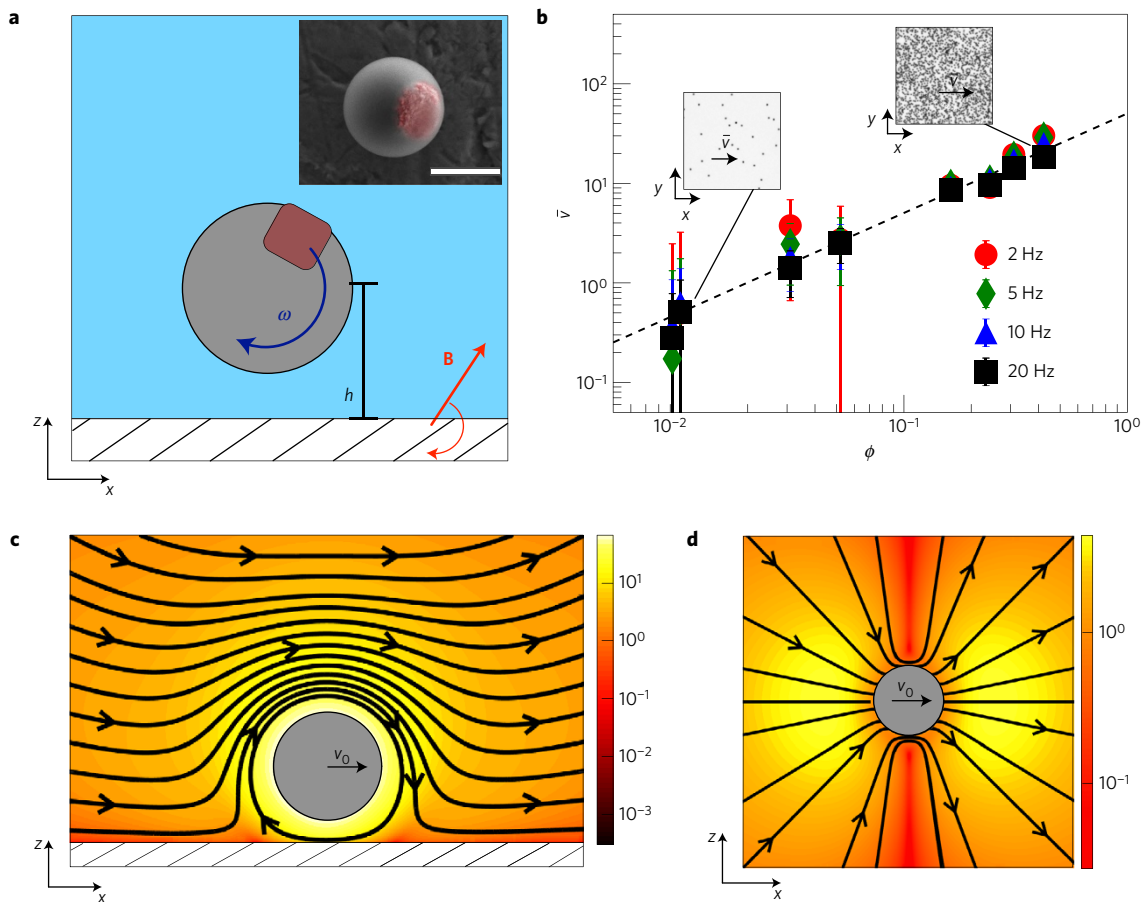
Figure 1 | Strong velocity enhancement due to collective effects. a, SEM and schematic of the polymer colloids with an embedded magnetic cube, indicated in red. Scale bar, 1 μm. A rotating magnetic field, **B**, with angular frequency ω directs particle motion. **b**, Normalized particle velocity measured in experiments, $\bar{v} = (v - v_0)/v_0$, versus area fraction, ϕ, at fixed field strength, $B_0 = 3$ mT, for various frequencies $f = \omega/2\pi$. Insets show pictures of the system at the highest and lowest ϕ. The best linear fit (dashed line) shows a strong dependence of $\bar{v}$ on ϕ, $\bar{v} = \alpha\phi$, where $\alpha = 50 \pm 2$. **c,d**, Calculated streamlines around a rotating particle ($f = 10$ Hz, $h = 0.98$ μm) in the plane perpendicular (**c**) and parallel (**d**) to the rotation direction. Flow velocity is normalized by single particle translation velocity v_0 and its magnitude is shown by the colour bar.

orders of magnitude slower than the fluid velocity at the particle's surface (ωa). The velocity field around a particle decays slowly (as $1/r^2$) in the xy-plane, where r is the distance to the particle centre. Thus, even at moderate area fractions, ϕ, particle motion is mainly a result of being advected in the flow of neighbouring particles. This collective effect can be described by a density-dependent mean velocity, $\bar{v} \equiv (v - v_0)/v_0 = \alpha\phi$, where α is found to be 50 ± 2 in our experimental system (see Fig. 1b). Putting $v \approx \alpha\phi v_0$ into the continuity equation,

$$\frac{\partial \phi}{\partial t} + \frac{\partial (v\phi)}{\partial x} = \frac{\partial \phi}{\partial t} + \alpha v_0 \frac{\partial (\phi^2)}{\partial x} = 0 \qquad (1)$$

results in the inviscid Burger's equation, which is well known to lead to the development of a shock front[21]. Although the development of a shock is a simple consequence of having a density-dependent velocity, to our knowledge, this feature has been observed only in low-density flowing emulsion systems[22,23], and not other colloidal roller systems[14]. As in Burger's solution, we need a leading edge density gradient to observe the shock.

The propagating shock front quickly becomes unstable in the direction transverse to propagation, leading to the appearance of density fluctuations which continue to grow as fingers (see Fig. 2a and Supplementary Movies 1 and 2). This fingering instability does not occur in a planar Burger's shock[24]. Both the experiments and simulations show a qualitatively similar evolution of the shock,

the shock instability, and the fingering, at the same relative times. Despite its deceptively similar appearance, this fingering instability is distinct from other previously reported viscous[11], granular[2,25] and colloidal instabilities[26–28]. In a Rayleigh–Taylor-like instability, the fingering dynamics is controlled by a balance of viscous damping and a body-force driving term (like gravity). In contrast, the instability wavelength in this system is independent of both viscosity and driving torque (that is, rotation rate); see Fig. 2b,c. We define the instability wavelength, λ_{max}, as the wavelength associated with the fastest growing normal mode, as is typical for a linear instability (see Supplementary Section III for details). The control parameter for this instability, in both the experiments and the simulations, is h, as illustrated in Fig. 2d,e. As shown in that figure, when the particle–wall distance increases, the instability wavelength increases linearly. The numerical results are obtained by confining the particles to a plane parallel to the wall at a given height h (see Supplementary Movie 3). As discussed later in the text, the same dynamics are observed in this configuration as in the fully three-dimensional (3D) simulations. In the experiments, the height is adjusted by changing the solvent density, and hence the colloids' buoyant weight mg. Although we change the particle–wall separation in quite different ways in the experiments and simulations, in both cases h is the key control parameter for λ_{max}.

Due to the increased density in the shock region, the fingertips are much denser and, due to collective effects, that is, $\bar{v} = \alpha\phi$, move much faster than the rest of the suspension. In the simulations,
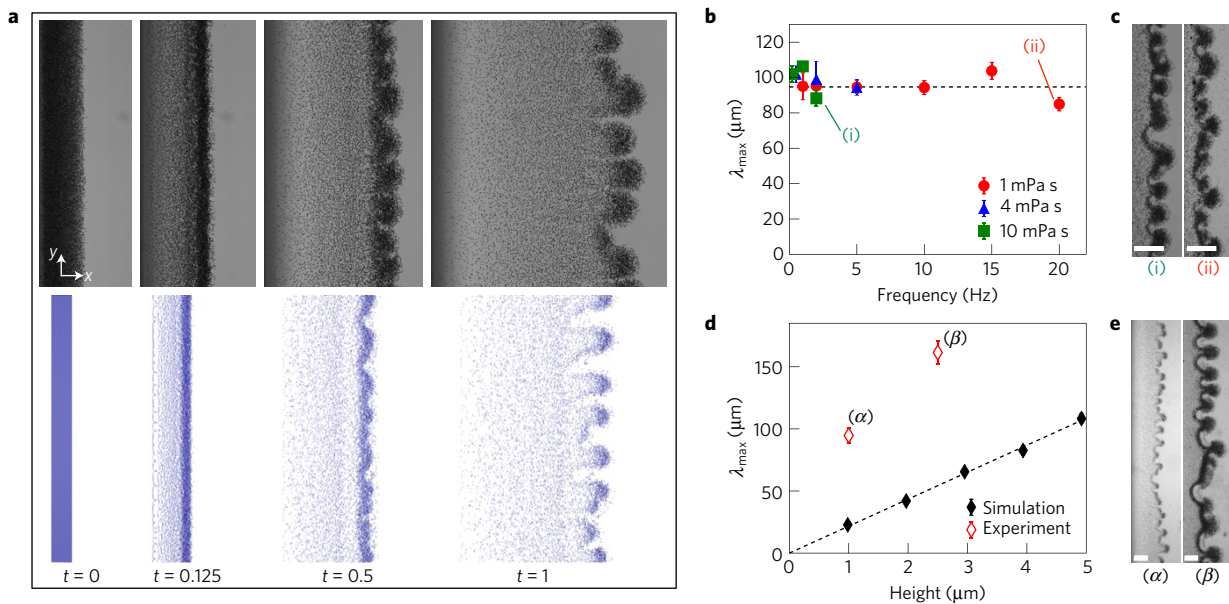
Figure 2 | Fingering instability. a, Instability in the experiment (above) and simulation (below) at the same relative points in time (in the xy-plane). Labels indicate scaled time (arbitrary units), and all images are 0.55 mm tall. **b**, Experimental data of instability wavelength, λ_{max} versus f, for three different fluid viscosities (different symbols), dashed line indicates mean λ_{max}. **c**, Experimental images corresponding to (i) $\eta = 1$ mPa s and (ii) $\eta = 10$ mPa s. Scale bar, 100 μm. **d**, Experimental and simulation data of λ_{max} versus h, dashed line indicates best linear fit to the simulation data. **e**, Experimental images for gravitational heights (α) $h = 1.0$ μm and (β) $h = 2.5$ μm. Scale bar, 100 μm. (All error bars represent standard error of the mean.)
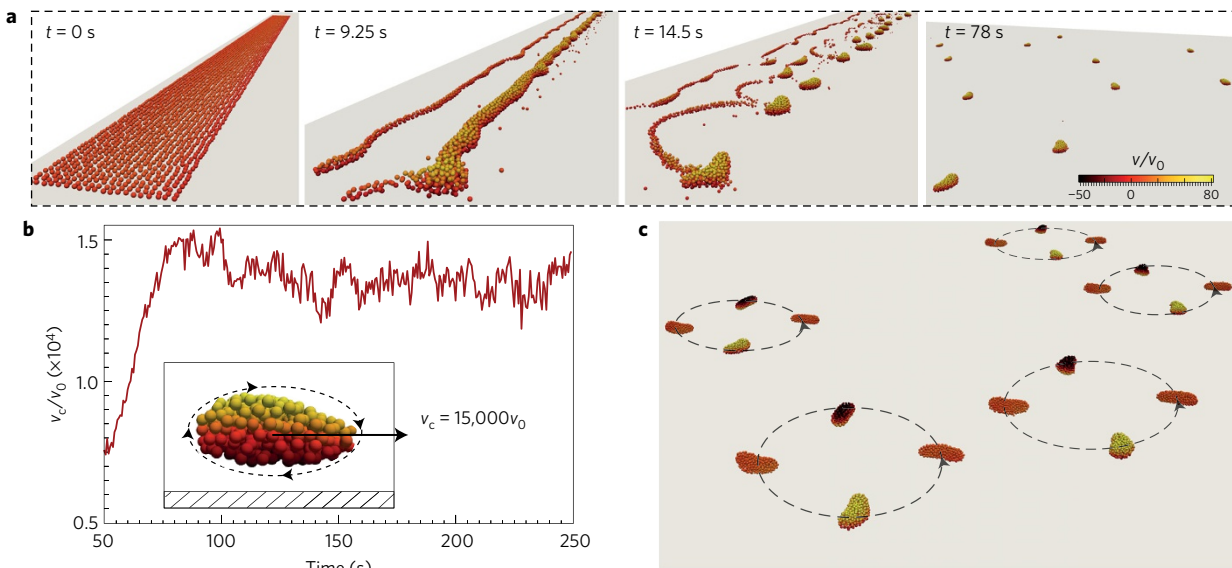
Figure 3 | Self-sustained critters. a, Time evolution of the instability. Colour bar indicates translational velocity in radii/s and the camera position changes dynamically. $t = 0$ s: 8,000 rollers are initially randomly distributed on a strip. $t = 9.25$ s: a compact front appears and starts to destabilize. $t = 14.5$ s: the fingertips start to detach from the front and form critters. $t \geq 78$ s: the critters reach a stable steady state in which they translate autonomously at a constant speed. **b**, Time evolution of normalized translational velocity of a critter, v_c/v_0, where v_0 is the velocity of a roller at the same centre of mass height. Inset: side view of the critter at $t = 78$ s, as indicated by the arrows, particles rotate about the centre of mass of the critter. **c**, Circular periodic trajectory of five critters rotating anticlockwise in response to slowly changing the axis of rotation. The period of the trajectory is $T = 40$ s and a frame is shown every $T/4$.

if the particles are maintained high enough away from the wall, the fingertips break off to form self-sustained, compact clusters made of hundreds of particles, which we term 'critters' (see Fig. 3a and Supplementary Movie 4). These critters rotate around their centre of mass and translate with a speed 15,000 times faster than a single roller would at the same centre of mass height (Fig. 3b inset). Critters form a natural stable state of the system: they move at a constant speed, do not lose particles, and are not

observed to dissolve (see Fig. 3b and Supplementary Movie 4). We further explore their stability by changing the direction (but not the magnitude) of ω periodically in time. As shown in Fig. 3c and Supplementary Movie 5, the critters follow the prescribed circular trajectory. Somewhat similar structures to the critters were obtained experimentally when h was increased (Fig. 2e and Supplementary Movie 6), although in the experiment critters continually lost some particles as they moved. In the simulations, the compact critters are
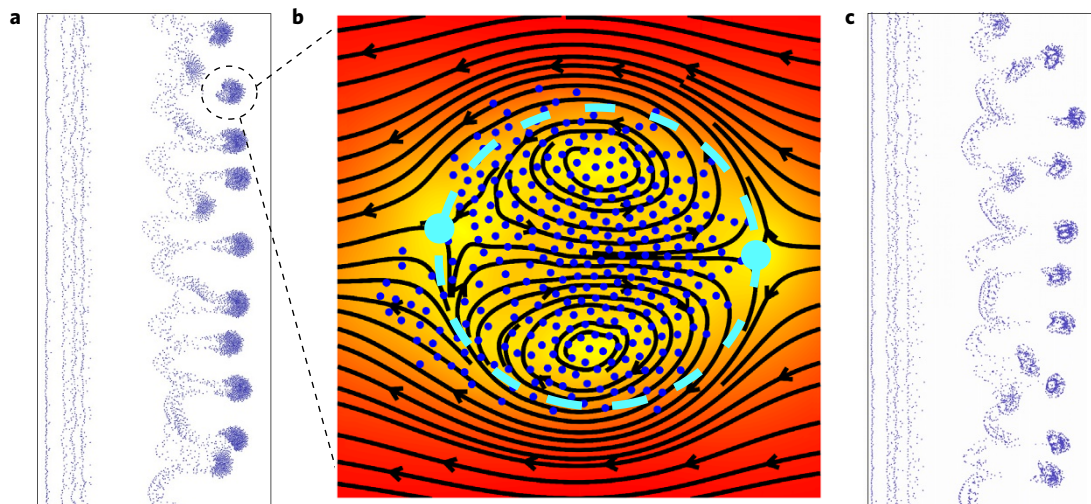
Figure 4 | Instability and clustering controlled by hydrodynamics. Simulations with rollers restricted to a plane $z = 3.94\,\mu m$, at time $t = 74$ s. **a**, Simulations include both steric interactions and finite size effects. **b**, Flow field in the frame moving with a cluster. Blue dots indicate roller positions, the dashed cyan line circles the recirculation zone where motion is self-sustained, and the cyan dots show the stagnation points. **c**, Purely hydrodynamic simulation of rotlet singularities with no steric repulsion reproduce the instability.

extremely robust, suggesting they may be an attractor in the system dynamics—similar critters appear regardless of the initial conditions (see Supplementary Movie 7).

The velocity field in Fig. 1d suggests that the transverse instability of the shock originates from the lateral hydrodynamic attraction and repulsion in the xy-plane; this lateral flow shows the same qualitative features for a rigid sphere and for a point rotlet above a no-slip boundary[9]. To test the assumption that this is a planar instability, we simplify the system in our simulations by restricting the rollers to a fixed plane above the wall. This simplified system reproduces the instability: the shock forms, the transverse instability develops, and autonomous clusters with selected size detach and translate much faster than individual particles, as shown in Fig. 4a. We further remove all non-hydrodynamic effects and simplify the system to its bare minimum by simulating instead a collection of point rotlet singularities without any steric repulsion. Figure 4c and Supplementary Movie 8 show that both the fingering instability and clustering are reproduced with only this one ingredient: hydrodynamic interactions in the vicinity of a no-slip boundary.

A closer look at the flow field around a cluster in the frame moving with its centre of mass shows a well-defined recirculation zone whose size matches the cluster size, as shown in Fig. 4b. The closed streamlines in this flow field are responsible for the self-sustained and compact clusters. As seen in studies of sedimenting particle clouds[29], the chaotic nature of the flow inside a cluster can lead to the loss of particles. However, in our 3D simulations, additional circulation in the xz-plane prevents particle loss; the critters are stabilized by the closed streamlines. Critters smaller than the size of the recirculation zone, which is proportional to the height above the wall, can form and remain stable, while larger ones break up by shedding excess particles.

Clustering is seen in many other low-Reynolds-number systems, from sedimentation to active colloidal particles. What is notable about the critters that emerge from this instability is that they are a persistent state which can be produced from hydrodynamic interactions. Other kinds of hydrodynamic clusters, such as those seen in sedimentation[30,31], are always transient and not long-lived structures. Almost all active matter systems exhibit some kind of clustering instability[3,4], but it is usually a consequence of particle–particle interactions, either directly through an attractive potential, sensing, or via self-trapping, which is a consequence of a repulsive particle potential. Here we have demonstrated that

the same instability observed in the experiments is preserved in the simulations, even when all interactions except hydrodynamics are removed.

In this study, we isolated the role of hydrodynamics. We note that this instability is generic and should be found in any system of particles rotating parallel to a floor, provided that hydrodynamics is the dominant particle–particle interaction. The addition of particle–particle potentials can strongly modify the instability structure and dynamics. For example, varying the Mason number (relative strength of hydrodynamic and magnetic interactions) completely changes the dynamics of the system (see Supplementary Section II and Supplementary Movie 9). The structures and flow patterns formed in our model system suggest a number of possible applications. Collections of rollers create strong advective flows, and their motion and direction can be externally powered and controlled. As shown in Supplementary Section IV, we have found, both experimentally and in simulations, a number of promising ways to transport passive particles by microrollers in either homogeneous suspensions, fingers, or critters.

Methods

Methods, including statements of data availability and any associated accession codes and references, are available in the online version of this paper.

References

1. Anderson, V. J. & Lekkerkerker, H. N. Insights into phase transition kinetics from colloid science. *Nature* **416**, 811–815 (2002).
2. Aranson, I. S. & Tsimring, L. S. Patterns and collective behavior in granular media: theoretical concepts. *Rev. Mod. Phys.* **78**, 641–692 (2006).
3. Marchetti, M. *et al.* Hydrodynamics of soft active matter. *Rev. Mod. Phys.* **85**, 1143–1189 (2013).
4. Palacci, J., Sacanna, S., Steinberg, A. P., Pine, D. J. & Chaikin, P. M. Living crystals of light-activated colloidal surfers. *Science* **339**, 936–940 (2013).
5. Bialké, J., Speck, T. & Löwen, H. Active colloidal suspensions: clustering and phase behavior. *J. Non-Cryst. Solids* **407**, 367–375 (2015).
6. Lu, P. J. & Weitz, D. A. Colloidal particles: crystals, glasses, and gels. *Annu. Rev. Condens. Matter Phys.* **4**, 217–233 (2013).
7. Schwarz-Linek, J. *et al.* Phase separation and rotor self-assembly in active particle suspensions. *Proc. Natl Acad. Sci. USA* **109**, 4052–4057 (2012).

8. Vicsek, T. & Zafeiris, A. Collective motion. *Phys. Rep.* **517,** 71–140 (2012).
9. Blake, J. & Chwang, A. Fundamental singularities of viscous flow. *J. Eng. Math.* **8,** 23–29 (1974).
10. Lee, S. & Leal, L. Motion of a sphere in the presence of a plane interface. Part 2. an exact solution in bipolar co-ordinates. *J. Fluid Mech.* **98,** 193–224 (1980).
11. Huppert, H. E. Flow and instability of a viscous current down a slope. *Nature* **300,** 427–429 (1982).
12. Chandrasekhar, S. *Hydrodynamic and Hydromagnetic Stability* (Oxford, 1961).
13. Sacanna, S., Rossi, L. & Pine, D. J. Magnetic click colloidal assembly. *J. Am. Chem. Soc.* **134,** 6112–6115 (2012).
14. Bricard, A., Caussin, J.-B., Desreumaux, N., Dauchot, O. & Bartolo, D. Emergence of macroscopic directed motion in populations of motile colloids. *Nature* **503,** 95–98 (2013).
15. Sing, C. E., Schmid, L., Schneider, M. F., Franke, T. & Alexander-Katz, A. Controlled surface-induced flows from the motion of self-assembled colloidal walkers. *Proc. Natl Acad. Sci. USA* **107,** 535–540 (2010).
16. Martinez-Pedrero, F., Ortiz-Ambriz, A., Pagonabarraga, I. & Tierno, P. Colloidal microworms propelling via a cooperative hydrodynamic conveyor belt. *Phys. Rev. Lett.* **115,** 138301 (2015).
17. Grzybowski, B. A., Stone, H. A. & Whitesides, G. M. Dynamic self-assembly of magnetized, millimetre-sized objects rotating at a liquid–air interface. *Nature* **405,** 1033–1036 (2000).
18. Snezhko, A. Complex collective dynamics of active torque-driven colloids at interfaces. *Curr. Opin. Colloid Interface Sci.* **21,** 65–75 (2016).
19. Swan, J. W. & Brady, J. F. Simulation of hydrodynamically interacting particles near a no-slip boundary. *Phys. Fluids* **19,** 113306 (2007).
20. Usabiaga, F. B. *et al*. Hydrodynamics of suspensions of passive and active rigid particles: a rigid multiblob approach. Preprint at http://arxiv.org/abs/1602.02170 (2016).
21. Burgers, J. *The Nonlinear Diffusion Equation: Asymptotic Solutions and Statistical Problems. Lecture series* (Springer, 1974).
22. Beatus, T., Tlusty, T. & Bar-Ziv, R. Burgers shock waves and sound in a 2D microfluidic droplets ensemble. *Phys. Rev. Lett.* **103,** 114502 (2009).
23. Desreumaux, N., Caussin, J.-B., Jeanneret, R., Lauga, E. & Bartolo, D. Hydrodynamic fluctuations in confined particle-laden fluids. *Phys. Rev. Lett.* **111,** 118301 (2013).
24. Goodman, J. & Miller, J. R. Long-time behavior of scalar viscous shock fronts in two dimensions. *J. Dyn. Differ. Equ.* **11,** 255–277 (1999).
25. Pouliquen, O., Delour, J. & Savage, S. Fingering in granular flows. *Nature* **386,** 816–817 (1997).
26. Pan, T., Joseph, D. & Glowinski, R. Modelling Rayleigh–Taylor instability of a sedimenting suspension of several thousand circular particles in a direct numerical simulation. *J. Fluid Mech.* **434,** 23–37 (2001).
27. Lin, T., Rubinstein, S. M., Korchev, A. & Weitz, D. A. Pattern formation of charged particles in an electric field. *Langmuir* **30,** 12119–12123 (2014).
28. Wysocki, A. *et al.* Direct observation of hydrodynamic instabilities in a driven non-uniform colloidal dispersion. *Soft Matter* **5,** 1340–1344 (2009).
29. Metzger, B., Nicolas, M. & Guazzelli, E. Falling clouds of particles in viscous fluids. *J. Fluid Mech.* **580,** 283–301 (2007).
30. Löwen, H. Particle-resolved instabilities in colloidal dispersions. *Soft Matter* **6,** 3133–3142 (2010).
31. Guazzelli, E. & Hinch, J. Fluctuations and instability in sedimentation. *Annu. Rev. Fluid Mech.* **43,** 97–116 (2011).

Author contributions

M.D. performed the experiments. B.D. performed the simulations. M.Y. and S.S. synthesized the colloidal particles. M.D., B.D., A.D. and P.C. conceived the project, analysed the results and wrote the paper.

Additional information

Supplementary information is available in the online version of the paper. Reprints and permissions information is available online at www.nature.com/reprints. Correspondence and requests for materials should be addressed to M.D. or B.D.

Competing financial interests

The authors declare no competing financial interests.

Methods

Experiments. The colloidal particles are TPM (3-methacryloxypropyl trimethoxysilane) spheres ($a = 0.66\,\mu m$) with haematite cubes embedded into them (see Sacanna *et al.*[13] for details of the synthesis). Haematite is a canted anti-ferromagnet, thus the particles possess a small permanent moment, $|\mathbf{m}| \sim 5 \times 10^{-16}\,A\,m^{-2}$, which can be oriented in an applied magnetic field. The particles are dispersed in either water or aqueous glycerol solutions (dynamic viscosity $\eta = 1\,mPa\,s$, $\eta = 4\,mPa\,s$, or $\eta = 10\,mPa\,s$). To increase buoyancy, additional samples are created with particles dispersed in a 410 mM sodium polytungstate solution, with a small amount of tetramethylammonium hydroxide (TMAH) added as an additional stabilizer (1.2% v/v).

In all cases, the particles are contained in glass capillary tubes of depth $100\,\mu m$ or greater (VitroCom VitroTubes), which are sealed with ultraviolet epoxy (Norland NOA63). To create the initial density gradient in particle concentration, the chambers are tilted so that particles gather to one side, then are laid flat to ensure a monolayer is formed as the initial condition. Distance of this initial gradient to the vertical chamber wall does not affect the instability wavelength.

The rotating magnetic field is created using custom triaxial coils. A bipolar current supply (KEPCO BOP 50-2M) is used to apply the current to the coils and create a rotating magnetic field. The waveforms for the rotating field are generated using a DAQ (MCC USB-3101FS) controlled via Matlab. The field generated by the coils is measured with a Hall sensor (Ametes MFS-3A). For all experiments described in this work, the magnitude of the field is 2.94 mT, and the frequency is varied from 0.2–25 Hz.

All observations are made using a Nikon Ti-U inverted microscope. Roller velocity is calculated in two ways. At low area fractions ($\phi < 0.1$), the velocity is computed using the instantaneous velocity calculated from particle tracking[32]. The velocity was computed for small segments of the individual particle tracks, and the results were then binned to calculate the mean roller velocity. At high area fractions, individual particle velocities cannot be measured, and a custom Python code was used to process the images and perform particle image velocimetry (PIV) analysis. The roller velocity was then taken to be the mean suspension velocity computed from the PIV analysis. Using a range of area fractions where both particle tracking and PIV could be used, $\phi = 0.10 - 0.20$, we validated that the mean suspension velocity matched the individual particle velocity—that is, when hydrodynamic collective effects are predominant, the mean suspension velocity is equivalent to the individual particle velocity.

Simulations. The flow fields around one roller shown in Fig. 1 are obtained by using the rigid multi-blob method developed by Usabiaga and colleagues[20]. The surface of the roller is discretized with 2,562 blobs which are rigidly connected with constraint forces. Pairwise hydrodynamic interactions between blobs are modelled with the Rotne–Prager–Blake tensor with wall corrections[19].

The multi-particle simulations are performed using the Stokesian Dynamics method developed by Swan and Brady[19], omitting stresslets and thermal fluctuations (Brownian motion). In brief, the hydrodynamic response is computed by replacing each sphere with a regularized singularity (stokeslet and rotlet) and accounting for the hydrodynamic interaction with the wall in an approximate but self-consistent way by applying Rotne–Prager corrections to the Blake image construction[9]. This modelling includes only leading-order corrections for the finite size of the particles to limit the computational cost required to simulate large numbers ($O(10^4)$) of particles. Even though this low-resolution model overestimates the particle mobility, it remains physically consistent, and its accuracy can be controlled and quantified. A better-resolved multi-blob model[20]

would increase the hydrodynamic accuracy but incur a higher computational cost. We compare both the minimally resolved model[19] and the well-resolved multi-blob model[20] with experiments in Supplementary Section I.

As in the experiments, the rotation rate of the particles is prescribed. This is ensured by applying the appropriate torques $\mathbf{T}$ obtained by solving the following resistance problem[19]

$$M^{rr}\mathbf{T} = \mathbf{\Omega} - M^{rt}\mathbf{F} \qquad (2)$$

where M^{rr} is the mobility matrix coupling the prescribed particle rotations $\mathbf{\Omega}$ to the unknown particle torques $\mathbf{T}$. M^{rt} is the mobility matrix coupling $\mathbf{\Omega}$ to the known external forces $\mathbf{F}$ acting on the particles, which are a combination of particle–particle and particle–wall repulsive forces and gravity. Once the torques are obtained, the translational velocities $\mathbf{V}$ are found with the mobility relation

$$\mathbf{V} = M^{tr}\mathbf{T} + M^{tt}\mathbf{F} \qquad (3)$$

where $M^{tr} = (M^{rt})^T$ couples $\mathbf{V}$ to $\mathbf{T}$ and M^{tt} couples $\mathbf{V}$ to $\mathbf{F}$. When the particles are restricted to a plane at fixed height $z = h$, forces and motion in the $\mathbf{z}$-direction are discarded. Particle trajectories are integrated with the two-step Adams–Bashforth–Moulton predictor–corrector scheme. The time step Δt is chosen so that a particle does not travel more than 5% of its size per time step: $v\Delta t < 0.05a$. Typically, $\Delta t = 0.005$ s in most of the simulations. Mobility-vector products and steric interactions are computed with PyCUDA on an Nvidia K40 GPU. The typical simulation time is 7 h for 20,000 time iterations with $O(10^4)$ particles.

When included, steric interactions between the particles are modelled with a pairwise soft-core repulsive potential U_{part} of Yukawa type,

$$U_{part}(r) = S_P \frac{a}{r} \exp\left(-\frac{r}{D_P}\right)$$

where r is the centre-to-centre distance between particles, S_P is the strength of the potential ($S_P = 2.43 \times 10^8\,mga$) and the interaction range is $D_P = 0.1a$. Since the simulations do not include Brownian motion, to balance gravity forces and set the equilibrium height of the particles we use a repulsive potential from the wall

$$U_{wall}(z) = S_w \frac{a}{z - a} \exp\left(-\frac{z - a}{D_w}\right)$$

where z is height of the particle centre. The strength S_w and the range D_w are changed between the simulations to investigate the effect of the particle height on the instability: $S_w = 0.05$–$25.1\,mga$ and $D_w = 0.1a$–$7a$. The total force on the particles $\mathbf{F}$ is given by the gradient of the combination of the repulsive potentials, U_{part} and U_{wall}, and the gravitational potential mgz, where $m = 1.27 \times 10^{-15}$ kg is the excess mass of a roller.

Data availability. The data that supports the plots within this paper and other findings of this study are available from the corresponding author on request.

References

32. Allan, D., Caswell, T., Keim, N. & van der Wel, C. trackpy: Trackpy v0.3.2 [Data set]. Zenodo. https://doi.org/10.5281/zenodo.60550 (2016).